Title: Spectroscopic Observation and Modeling of Photonic Modes in CeO_2 Nanostructures

Running title: Spectroscopic Study on Photonic Modes in CeO_2

Authors: Yifan Wang[1], Shize Yang[2], and Peter A. Crozier[1]*

Primary Institution: Arizona State University

Affiliations and Address:

1. School for Engineering of Matter, Transport & Energy, Arizona State University, Tempe, AZ, 85287, United States.

2. Eyring Materials Center, Arizona State University, Tempe, AZ, 85287, United States.

***Corresponding Author Email**: crozier@asu.edu

Conflict of Interest:

All authors declare that they have no conflicts of interest.

Abstract

Photonic modes in dielectric nanostructures, e.g., wide gap semiconductor like CeO_2 (ceria), have the potential for various applications such as information transmission and sensing technology. To fully understand the properties of such phenomenon at the nanoscale, electron energy-loss spectroscopy (EELS) in a scanning transmission electron microscope (STEM) was employed to detect and explore photonic modes in well-defined ceria nanocubes. To facilitate the interpretation of the observations, EELS simulations were performed with finite-element methods. The simulations allow the electric and magnetic field distributions associated with different modes to be determined. A simple analytical eigenfunction model was also used to estimate the energy of the photonic modes. In addition, by comparing various spectra taken at different location relative to the cube, the effect of the surrounding environment on the modes could be sensed. This work gives a high-resolution description of the photonic modes' properties in nanostructures, while demonstrating the advantage of EELS in characterizing optical phenomena locally.

Introduction

Photonic modes, sometimes referred as cavity modes or waveguide modes, is a phenomenon in some dielectric materials, with specific sizes and shapes in which photons may form a standing wave and be temporarily trapped or channeled in the material. Such modes have been widely applied in fields such as telecommunication (Ramp et al., 2020; Schatzl et al., 2017), laser generation (Morville et al., 2005; Painter et al., 1999) and sensors (Gan et al., 2017; Lucklum et al., 2012). When the size of the structure is on the order of a few hundred nanometers, photonic modes associated with visible light can form, enabling potential application to fields such as energy conversion and sensing (Dong et al., 2007; Ge et al., 2013; Luo et al., 2015).

To fully tap the potential of photonic modes in nanostructures, a deeper understanding of the modes' properties is needed. However, despite high energy resolution, traditional optical measurement methods, e.g., Raman spectroscopy (McCreery, 2001) and infrared spectroscopy (Stuart, 2004), usually suffer from low spatial resolution, of around 1 micrometer. An alternative approach to trigger and locally

probe photonic modes in nanostructure is to employ high energy focused electron beams which have dimensions of 0.1 nm or less. For a free electron beam, the electric field in frequency space can be described in terms of virtual photons (Jackson, 1999). In the case of scanning transmission electron microscopy (STEM), the high energy electron probe can act as a sub-nanometer source that emits continuum light that has a component perpendicular to the beam propagation direction.

With the advances in electron optics, especially aberration corrector (Haider et al., 1998; Krivanek et al., 1999), monochromator (Krivanek et al., 2009; Tiemeijer et al., 2001), and detectors (Eisenstein et al., 2019; Plotkin-Swing et al., 2020), studying low-energy phenomena including plasmonic (Koh et al., 2009; Schaffer et al., 2010; Wu et al., 2018) and phononic (Hachtel et al., 2019; Hage et al., 2017, 2018, 2019, 2020; Hoglund et al., 2022; Krivanek et al., 2014; Lagos et al., 2017; Venkatraman et al., 2019; Yan et al., 2021) response at atomic resolution with adequate energy resolution (~10meV) through electron energy-loss spectroscopy (EELS) in STEM is feasible. These enhancements in the quality of EELS in the electron microscope also enable photonic modes to be explored with higher energy resolution compared to the past.

Previous studies on photonic modes in silicon-based materials with different shapes supported by thin films has shown that STEM-EELS as a powerful tool to explore this phenomenon (Alexander et al., 2021; Kordahl et al., 2021; Yurtsever et al., 2008). Such studies provided a deep understanding of the modes and more recent investigations have focused on wider band-gap materials with different shapes, e.g., CeO_2, and TiO_2 nanoparticles (Liu et al., 2019). Also, it shown that the modes are easier to detect at higher accelerating voltage in the aloof beam geometry. However, many nanoparticle systems have complex aggregate geometries which may impact the character of photonic modes especial if there is strong coupling. The photonic response from such complex systems is not easy to model and must be explored with experimental approaches. High spatial resolution EELS is ideally suited to investigating the heterogeneity in the photonic response in nanoscale systems with complex geometry.

In this paper, STEM-EELS was performed on well-defined cerium oxide nanocubes. Through energy-loss spectra and mapping, different mode excitation due to the geometry difference are demonstrated, i.e., some modes may be more preferentially excited when the beam is placed at specific positions. To

further understand such spatial variations in mode excitation, numerical finite element calculation was performed in the commercial software COMSOL Multiphysics and compared with a simple analytical model to calculate the energy of photonic modes in cubic nanoparticles with given dielectric functions. The influence of the surrounding environment on the properties of photonic modes is also investigated. In particular, the change in the character of the photonic modes when there is strong coupling with surrounding aggregate is explore.

Methods

Synthesis

Ceria nanocubes with predominantly (100) surface terminations were synthesized using a hydrothermal method (Yang et al., 2007). Cerium nitrate hexahydrate ($Ce(NO_3)_3 \cdot 6H_2O$) and sodium hydroxide (NaOH) were separately dissolved in deionized water. The solution was mixed and stirred using a magnetic stirrer for 30 min. The final molar concentration of NaOH was calculated to be 8 M. In order to get cubes with ideal size for photonic modes, the mixture was heated inside an autoclave at 220°C for 24 hours and cooled down in 1 hour. The precipitate particles that formed were dispersed in deionized water by sonicating for 20 min. The top layer of the suspension was used for TEM observation by drop-casting onto a lacey carbon film supported on Cu grids. The sample was baked at 150ºC for two hours to avoid carbon contamination.

STEM and EELS measurements

Monochromated-EELS was performed with NION UltraSTEM 100 microscope equipped with an aberration corrector and the state-of-the-art Dectris ELA detector (Plotkin-Swing et al., 2020). The microscope was operated at 100 kV. The energy dispersion of the spectrometer was set to 5 meV per channel and the measured zero-loss peak full width half maximum was 18 meV. The convergence and collection semi angle of the experiment were set to 19 mrad and 21.8 mrad respectively, (a 2 mm spectrometer entrance aperture was employed), giving a probe size of 120 pm. To increase the signal-to-noise ratio (SNR), 100 spectra taken at the same position with 500 ms exposure time and subsequently summed. EELS mapping was also performed from ceria cubes and surrounding areas with

a dwell time of 100 ms per pixel to minimize the effect of sample drift while maintaining an adequate SNR. Maps were plotted as the background-subtracted intensity at each major peak energy with a 5meV window (1 pixel width on the spectrometer). The data was processed with Nion Swift and Gatan Digital Micrograph. The background subtraction is described in **supplement S1**.

Finite element simulations

Finite element methods were employed to simulate the energy-loss spectra. The calculations were performed with the radio frequency module in COMSOL Multiphysics, which has been previously employed for the plasmonic (Raza et al., 2014; Wiener et al., 2013) and vibrational loss (Konečná et al., 2018) spectral region. Electric fields corresponding to different frequencies can be derived from solutions of Maxwell's equations. The energy-loss probability can be evaluated through the following equation (Konečná et al., 2018):

$$\Gamma_{EELS}(\omega) = \frac{e}{2\pi\hbar\omega}\int dz Re[E_z^{ind}(z,\omega)e^{-\frac{i\omega z}{v}}]$$

where v, e, ω, E^{ind} are the velocity of electron, unit charge, frequency and induced electric field, and z is the propagating direction of the electron beam, respectively. The cerium oxide dielectric function was taken from the literature (Järrendahl & Arwin, 1998),

Result and Discussion

Energy-loss spectra and mappings

Measurements were performed on cubes that had faces both with and without aggregates present. A ceria nanocube with a size of around 200nm in a [100] orientation is shown in the high-angle annular dark-field (HAADF) image of **Figure 1a**. One face of the cube is nearly clean (i.e., aggregate free) while the other faces have differing degrees of contact with small and large aggregates. Spectra can be recorded in either aloof or transmission geometry, depending on whether the beam is located in the surrounding vacuum or is transmitting through the particle. In the aloof beam geometry, the energy-loss signal is generated as a result of delocalized electron-solid interactions (Crozier, 2017). The influence

of the distance from the electron beam to the crystal surface, defined as the impact parameter b (b>0 for aloof and b<0 for transmission geometries), on the aloof spectral intensity has been discussed previously in the literature (Howie & Milne, 1985; Liu et al., 2017).

In the aloof geometry, as the beam approaches the particle surface, the spectral intensity rises, with the peaks becoming most intense when the electron beam is positioned on the surface. This strong increase in the signal with decreasing impact parameter is expected for the aloof geometry. However, once the beam enters the CeO_2 cube, a pronounced reduction in overall spectral intensity is observed. This overall intensity drop in the transmission spectra is mainly because a significant portion of the incident electrons now undergo elastic scattering outside the spectrometer entrance aperture (Egerton, 2014). In practice, the visibility of the photonic modes is enhanced when the probe is close to the edge of the particle in the aloof beam geometry. Considering the convergent electron probe and the average nanoparticle thickness (~100-200 nm), the optimum impact parameter to observe the spectral signatures of photonic modes while avoiding elastic scattering contributions is 10 nm.

Figure 1b shows spectra from two different probe geometries: the blue one, denoted as the edge (**E**) position, is near the top left edge of the cube which is parallel to the direction of the incident electron beam, and the red one, denoted as the face (**F**) position, is around the middle of the face of the cube. Four major peaks between 2 eV and the bandgap edge (~3.40eV), denoted as peak **E1**(~2.45eV), **F1**(~2.65eV), **F2**(~3.10eV), and **E2**(~3.25eV), are present in the spectra. In the face position geometry, peaks **F1** and **F2** are the predominant peak, while peak **E2** is about half the intensity of peak **F2**, and peak **E1** is almost invisible. For the edge position, peaks **E1** and **E2** are stronger signal compared to face position, while there is a peak **F1*** of low intensity that has energy very close to peak **F1**, and peak **F2** is covered by the tail of peak **E2**.

Figure 2 presents the background-subtracted EELS intensity mapping of each major peak across the cube. In the transmission part of the map (i.e., on the cube), the intensity is a factor of 200 lower compared to the aloof geometry, due to elastic scattering as described above. We could compensate for elastic scattering by normalizing the maps to the total spectral intensity, but this was not done due to the very poor SNR associated with the transmitted signal. (It should be mentioned that there is no

Begrenzung effects for photonic modes because the imaginary part of the dielectric function is zero below the bandgap.) However, the photonic modes are still detectable in transmission as shown in **supplement S2**. Elastic scattering from small particles decorating the surface of the cube (see figure 1a) also causes some medium-low intensity contrast in the maps. For peak **F1** and **F2**, the high intensity region formed an arc-shape area, and the brightest area is at the center of the arc, close to the middle of the (100) surface. Meanwhile, peak **E1** and peak **E2** give higher intensity near the edge of the cube, especially the top left and bottom right. Also, peaks **E1** and **E2** are more strongly excited around the edge of the cube while modes corresponding to peaks **F1** and **F2** are more strongly excited at the middle of the face. The similarities between the **F** peak maps indicates that they have similar excitation probability distributions. The same applies to the **E** peak maps. (It should be noted that all the modes are excited at the same time when beam is placed at different positions, which just alter exciting probability of different modes.)

Finite element simulations of energy-loss spectra and standing wave model

To further understand the photonic modes in the cube, we performed numerical simulations with COMSOL Multiphysics. The geometry for the simulation is shown in **figure 3a** and was similar to the experiment set-up with an incident electron energy of 100 keV. We use a line current to simulate the electron beam, which is positioned 10 nm away from the cube and along z-direction in our Cartesian coordinate system. The beam was placed at the same position as the experimental edge and face settings. The simulated energy-loss spectra are plotted as **figure 3b**. The energy-loss spectra of two geometries show a very good qualitative match with the experimental spectra: the position of the valence loss edge is roughly the same, and the major four peaks and a minor peak **F1*** and their relative intensity agrees with that of experiment. The reason for slight differences between experiment and simulation might come from: (1) The dielectric data we use for simulation, which is measured from a film, may not exactly match that for our cube. (2) The assumption we made that the nanoparticle is a cube, which may not be true since we cannot measure the side of the particle that parallel to the beam. (3) In the experimental case, the cube surfaces are decorated with small nanoparticles and aggregates which are not included in the simulation. (4) The electron beam was modeled as a line current in COMSOL,

instead of convergent cones in real experiment, which leads to finer and sharper peaks in simulation (5) COMSOL assumes perfectly sharp edges, which is not true in reality. (6) The experimental spectra can be considered as the convolution of our simulated result and the ZLP, thus resulting in broader peaks that will cover potential minor features (Kimoto et al., 2005).

Another way to understand these modes is the basic standing wave model (Balanis, 2012):

$$\omega_{mnl} = \frac{\pi}{\sqrt{\mu\epsilon(\omega)}}\left(\frac{m^2}{a^2}+\frac{n^2}{b^2}+\frac{l^2}{c^2}\right)^{1/2} = \frac{\pi}{\sqrt{\mu\epsilon(\omega)}}\frac{k}{a},\ \ where\ k = \sqrt{m^2+n^2+l^2}$$

where $\omega, \mu, \epsilon, a, b, c$ are the frequency of the mode, the permeability (which we consider as a constant), the dielectric function in frequency, and three dimensions of the rectangular cuboid respectively. m, n, l are non-negative integers, which stands for the wave mode for each direction. Since it is a cube, a, b, c are the same and $a = 200nm$. In this case, the solution to this equation over the energy range of interest is given in **table 1a** (**Supplement S3** shows the detailed solving procedure). Notice that $k^2 = 7$ is skipped, which is because 7 cannot be written as the summation of three square of integers. There is a reasonable agreement between the peak energy generated by COMSOL simulations (**table 1b**) and the photonic eigenmode model. The reason for discrepancy between the two approaches is because, in the eigenfunction model, it is assumed that there is no penetration of the electromagnetic field beyond the cube boundaries, which is not true in both finite-element simulation and experiment (some field always extends beyond the cube boundary).

This equation also frames general conditions for photonic mode generation. The bandgap value will act as an upper limit of photonic mode energy (or the lower limit of photonic mode wavelength), since photons with energy larger than bandgap will be absorbed and the form electron-hole pairs. The real part of the dielectric function will determine the minimum size of the particle that can support a photonic mode. In a high-κ dielectric with a bandgap of 3~5eV bandgap like ceria, we can observe photonic modes in particles larger than 100 nm in size.

Electric field of the modes

An intuitive way to visualize the modes is to plot the time-integrated electric fields in the cube with each excitation geometry in frequency domain. We calculate the electric field in the cube for each peak energy. **Figure 4** shows the z components of electric field. The 3D plot of electric field shows standing wave patterns in the cube. To further visualize the modes, we plotted the cross section of the cube which has highest electric field intensity for each mode. For low energy modes (peak **E1** and **F1**), the highest intensity is in the middle of the cube, while it is low or even zero at some locations on the top and bottom surfaces. Higher energy modes give strong electric fields at the 1/4 and 3/4 height of the cube, and has weak field at middle, top and bottom of the field. (See **supplement S5** for field at other heights). Also, for the cross-section of the same energy at different heights, while the shape of the field is nearly identical, the sign of the field reverses as shown in **figure 4c-d**. The behavior in the z-direction indicates a periodicity of the electric field: a half period for lower energy peaks, and a full period for higher energy peaks.

Apart from the variation in z-direction, the electric field also shows specific symmetry for two different probe geometries. The electric field maps of the two edge peaks show a symmetry along the diagonals, while for the face geometry, the symmetry axis is the horizontal or vertical bisector line. The shape of the electric field also indicates the wave vector of the mode, especially for the edge modes: a wave pattern is formed in the diagonal direction. In addition, an energy comparison can be done with the estimation of wavelength based on the electric field pattern. Peak **E1** has a wavelength proportional to the diagonal of the square, thus the energy is lower than peak **F1**, of which the wavelength is around the side of the cube. For peak **F1** and **F2**, although they share similar electric field patterns in the x-y plane, peak **F2** has a shorter wavelength due to the extra half period in z-direction, and therefore a higher energy. The wavelength of peak **E2** in x-y plane is two third of the diagonal, which is shorter than the side of the cube by a little amount. This matches the fact that the energy of peak **E2** is slightly higher than peak **F2**.

Modes' properties with different surrounding environments

Notice that the peaks' intensities in the map do not show perfect spatial symmetry in **Figure 2**, for example, the map for peak **E2**. To understand the slight asymmetry, we acquired multiple spectra at different points along the side of the cube and extracted signals at points that would be symmetrically equivalent in terms of the geometry of a hypothetical clean cube. **Figure 5** shows two sets of 3 spectra at symmetrically equivalent points (with respect to perfect cube) and they show unexpected differences in major peaks between points, (matching the intensity variation of the EELS mapping). For face position (**figure 5b**), spectra at $\mathbf{F_L}$ and $\mathbf{F_R}$ are giving qualitatively similar results as the face position spectrum in **figure 1b**, while $\mathbf{F_B}$ shows an intensity decrease and peak broadening for both peak II and III. Similar results are observed at the edge positions (**figure 5c**): $\mathbf{E_{TL}}$ and $\mathbf{E_{BR}}$ are equivalent to the edge position results in **figure 1b**, whereas peak **E1** and especially, peak **E2** are suppressed when beam is placed at $\mathbf{E_{BL}}$. Although two sets of points are geometrically equivalent for a clean cube, the surrounding environment of the cube, e.g., the aggregates attached to the cube, is not symmetric.

There are two groups of aggregates that can possibly lead to a disturbance of the photonic modes: (1) small particles decorated the cube surfaces (2) a very large aggregate at the top and upper right side of the cube (see **Figure 1a**). According to the HAADF image, $\mathbf{E_{TL}}$, $\mathbf{F_B}$ and $\mathbf{F_R}$ are the three probe positions that are closer to the small particles on the surface. At these positions, the conduction band signal is stronger and shows a steeper rise due to the closer proximity of the probe to the small ceria particles. However, despite the fact that these three points collect additional signal from small particles, only $\mathbf{F_B}$ shows damping of the photonic peak intensity, which confirms that the asymmetry in the excitation of photonic modes is not simply caused by the small aggregates on the surface of the cube near the electron beam. On the other hand, we can see that modes generated from $\mathbf{E_{BL}}$ and $\mathbf{F_B}$ have a boundary associated with large aggregates with dimensions larger than the cube (see **Figure 1a**). This allows the photonic mode to couple into the adjacent aggregates and changes the resonant frequencies. (For more information on coupling the reader is referred to Liu et al (Liu et al., 2019)). These observations demonstrate that the variations in spectra from photonic modes are caused by the large aggregates at the top right side of the cube.

To aid the understanding in the origin of the change of the intensity and broadening of the peaks, it is useful to look at a simple classical behavior of the peaks in a spectrum. A peak can be described by its mode energy (E), integrated intensity ($\int IdE$, where I is the intensity), which is proportional to total number of photons generated, and characteristic width (ΔE). By time-energy uncertainty relation $\Delta E \Delta t \simeq \hbar$, a broad peak (large ΔE) means that the lifetime of the mode (Δt) will be short. Therefore, in terms of lifetime, the photonic modes decays much faster when the beam was placed at the point $\mathbf{E_{BL}}$ and $\mathbf{F_B}$ than $\mathbf{E_{TL}}$, $\mathbf{E_{BR}}$, $\mathbf{F_L}$ and $\mathbf{F_R}$ according to **figure 5**. From the simple case of Fresnel laws, when an electromagnetic (EM) wave travels normal to the interface, the reflected coefficient (R) and transmitted coefficient (T) of two linear media are (Griffiths, 2017):

$$R \equiv \left(\frac{n_1 - n_2}{n_1 + n_2}\right)^2 \quad T \equiv \frac{4n_1 n_2}{(n_1 + n_2)^2}\ , \ \ R + T = 1,$$

where n_1 is the refractive index of the medium that the EM wave comes from, and n_2 is the refractive index of the adjacent medium. If the two refractive indices are close to each other, R will be close to 0 while T will be close to 1, which means most of the wave will be transmitted through the interface instead of reflecting back from the interface. For cavity modes, a larger R, will increase the probability that the photon will be reflected from the surface, thus causing internal reflection and light trapping inside the nanocube. Thus, the standing wave formed has a longer lifetime, which will lead to a sharper peak in the spectra. According to Maxwell Garnett effective medium theory, the average dielectric function of the large cluster (including vacuum) can be approximated as (Bohren & Huffman, 1998):

$$\epsilon_{avg} = \epsilon_{vac}[1 + \frac{3f\left(\frac{\epsilon_{CeO_2} - \epsilon_{vac}}{\epsilon_{CeO_2} + 2\epsilon_{vac}}\right)}{1 - f\left(\frac{\epsilon_{CeO_2} - \epsilon_{vac}}{\epsilon_{CeO_2} + 2\epsilon_{vac}}\right)}]$$

where $\epsilon_{avg}, \epsilon_{vac}, \epsilon_{CeO_2}, f$ are the dielectric function of the cluster, vacuum and ceria, and the volume fraction of ceria respectively. From this equation we know that the average refractive index of the cluster will lie between the refractive index of vacuum and pure ceria. Thus, for waves travelling to the large cluster, i.e., modes generated when the electron beam is positioned at $\mathbf{E_{BL}}$ and $\mathbf{F_B}$, will decay faster due to higher probability of energy transmission to the clusters. When the beam is placed at $\mathbf{E_{TL}}$ and $\mathbf{E_{BR}}$,

most energy will reflect thus forming an intense standing wave, giving a sharper peak in EELS (**figure 3c**). For the $\mathbf{F_L}$ and $\mathbf{F_R}$, although the right surface is not perfectly clean, the thickness of the agglomerate layer is much smaller compared to both the size of the cube and the size of the large cluster above the cube. Thus, coupling to clusters is rather small and there is a higher possibility for the wave to be trapped in modes associated with the clean cube. Notice that the ability to sense a large aggregate on the face far from the electron beam demonstrates the potential of employing photonic modes in sensing applications.

Conclusion

The photonic modes in a well-defined ceria nanocube have been investigated using STEM-EELS. By placing the beam at different positions around the cube (e.g., edge sites and face sites), the existence of different modes and the variations in peak intensity was detected. EELS simulations through numerical calculation in COMSOL Multiphysics qualitatively agreed with the experiments. A simple standing wave model gave photonic eigenmodes of the cube based on particle size and dielectric function, which qualitatively agrees with the numerical simulations The finite-element calculation also provides electric field distribution in the cube. The field shows a standing wave pattern with wave vectors corresponding to different beam positions, i.e., a diagonal wave vector corresponds to edge positions, and a wave vector parallel to the side of the cube is generated from the face positions. The slight asymmetry of the surrounding environment of the nanocube, i.e., the small and large aggregates attached to the cube, is also utilized to demonstrate the transmission properties of photonic modes. Photonic modes associated with a clean cube will be suppressed in the presence of large aggregates that have a size comparable with the cube. In this case, energy will be transmitted to those clusters rather than being trapped in the cube. This work will provide guidance for engineering the energy of photonic modes and, also demonstrate EELS as a powerful tool to explore local response in photonic structures.

Acknowledgements

We acknowledge the financial support from the U.S. Department of Energy (grant no. BES DE-SC0004954) and U.S. National Science Foundation (grant no. CHE 2109202). We also acknowledge the use of (S)TEM at John M. Cowley Center for High-Resolution Electron Microscopy in the Eyring Materials Center at Arizona State University. We also gratefully thank the insightful discussions with Prof. Kevin Schmidt at ASU's Department of Physics on the interpretation of calculation results.

References

Alexander, D. T. L., Flauraud, V., & Demming-Janssen, F. (2021). Near-Field Mapping of Photonic Eigenmodes in Patterned Silicon Nanocavities by Electron Energy-Loss Spectroscopy. *ACS Nano*, *15*(10), 16501–16514. https://doi.org/10.1021/acsnano.1c06065

Balanis, C. A. (2012). *Advanced Engineering Electromagnetics* (Vol. 148). John Wiley & Sons, Inc.

Bohren, C. F., & Huffman, D. R. (1998). *Absorption and Scattering of Light by Small Particles*. Wiley. https://doi.org/10.1002/9783527618156

Crozier, P. A. (2017). Vibrational and valence aloof beam EELS: A potential tool for nondestructive characterization of nanoparticle surfaces. *Ultramicroscopy*, *180*, 104–114. https://doi.org/10.1016/j.ultramic.2017.03.011

Dong, X., Tam, H. Y., & Shum, P. (2007). Temperature-insensitive strain sensor with polarization-maintaining photonic crystal fiber based Sagnac interferometer. *Applied Physics Letters*, *90*(15), 151113. https://doi.org/10.1063/1.2722058

Egerton, R. F. (2014). Choice of operating voltage for a transmission electron microscope. *Ultramicroscopy*, *145*, 85–93. https://doi.org/10.1016/j.ultramic.2013.10.019

Eisenstein, F., Danev, R., & Pilhofer, M. (2019). Improved applicability and robustness of fast cryo-electron tomography data acquisition. *Journal of Structural Biology*, *208*(2), 107–114. https://doi.org/10.1016/j.jsb.2019.08.006

Gan, X., Zhao, C., Yuan, Q., Fang, L., Li, Y., Yin, J., Ma, X., & Zhao, J. (2017). High performance graphene oxide-based humidity sensor integrated on a photonic crystal cavity. *Applied Physics Letters*, *110*(15), 151107. https://doi.org/10.1063/1.4980045

García de Abajo, F. J. (2010). Optical excitations in electron microscopy. *Reviews of Modern Physics*, *82*(1), 209–275. https://doi.org/10.1103/RevModPhys.82.209

Ge, Y., Liu, Q., Chang, J., & Zhang, J. (2013). Optical fiber sensor for temperature measurement based on Silicon thermo-optics effect. *Optik*, *124*(24), 6946–6949. https://doi.org/10.1016/j.ijleo.2013.05.156

Griffiths, D. J. (2017). *Introduction to Electrodynamics* (Vol. 148). Cambridge University Press. https://doi.org/10.1017/9781108333511

Hachtel, J. A., Huang, J., Popovs, I., Jansone-Popova, S., Keum, J. K., Jakowski, J., Lovejoy, T. C., Dellby, N., Krivanek, O. L., & Idrobo, J. C. (2019). Identification of site-specific isotopic labels by vibrational spectroscopy in the electron microscope. *Science*, *363*(6426), 525–528. https://doi.org/10.1126/science.aav5845

Hage, F. S., Hardcastle, T. P., Scott, A. J., Brydson, R., & Ramasse, Q. M. (2017). Momentum- and space-resolved high-resolution electron energy loss spectroscopy of individual single-wall carbon nanotubes. *Physical Review B*, *95*(19), 1–11. https://doi.org/10.1103/PhysRevB.95.195411

Hage, F. S., Kepaptsoglou, D. M., Ramasse, Q. M., & Allen, L. J. (2019). Phonon Spectroscopy at Atomic Resolution. *Physical Review Letters*, *122*(1), 16103. https://doi.org/10.1103/PhysRevLett.122.016103

Hage, F. S., Nicholls, R. J., Yates, J. R., McCulloch, D. G., Lovejoy, T. C., Dellby, N., Krivanek, O. L., Refson, K., & Ramasse, Q. M. (2018). Nanoscale momentum-resolved vibrational spectroscopy. *Science Advances*, *4*(6), eaar7495. https://doi.org/10.1126/sciadv.aar7495

Hage, F. S., Radtke, G., Kepaptsoglou, D. M., Lazzeri, M., & Ramasse, Q. M. (2020). Single-atom vibrational spectroscopy in the scanning transmission electron microscope. *Science*, *367*(6482), 1124–1127. https://doi.org/10.1126/science.aaz5312

Haider, M., Uhlemann, S., Schwan, E., Rose, H., Kabius, B., & Urban, K. (1998). Electron microscopy image enhanced. *Nature*, *392*(6678), 768–769. https://doi.org/10.1038/33823

Hoglund, E. R., Bao, D. L., O'Hara, A., Makarem, S., Piontkowski, Z. T., Matson, J. R., Yadav, A. K., Haislmaier, R. C., Engel-Herbert, R., Ihlefeld, J. F., Ravichandran, J., Ramesh, R.,

Caldwell, J. D., Beechem, T. E., Tomko, J. A., Hachtel, J. A., Pantelides, S. T., Hopkins, P. E., & Howe, J. M. (2022). Emergent interface vibrational structure of oxide superlattices. *Nature*, *601*(7894), 556–561. https://doi.org/10.1038/s41586-021-04238-z

Howie, A., & Milne, R. H. (1985). Excitations at interfaces and small particles. *Ultramicroscopy*, *18*(1), 427–433. https://doi.org/10.1016/0304-3991(85)90161-5

Jackson, J. D. (1999). Classical Electrodynamics, 3rd ed . In *American Journal of Physics*. John Wiley & Sons, Inc.

Järrendahl, K., & Arwin, H. (1998). Multiple sample analysis of spectroscopic ellipsometry data of semi-transparent films. *Thin Solid Films*, *313–314*, 114–118. https://doi.org/10.1016/S0040-6090(97)00781-5

Kimoto, K., Kothleitner, G., Grogger, W., Matsui, Y., & Hofer, F. (2005). Advantages of a monochromator for bandgap measurements using electron energy-loss spectroscopy. *Micron*, *36*(2), 185–189. https://doi.org/10.1016/j.micron.2004.11.001

Koh, A. L., Bao, K., Khan, I., Smith, W. E., Kothleitner, G., Nordlander, P., Maier, S. A., & Mccomb, D. W. (2009). Electron energy-loss spectroscopy (EELS) of surface plasmons in single silver nanoparticles and dimers: Influence of beam damage and mapping of dark modes. *ACS Nano*, *3*(10), 3015–3022. https://doi.org/10.1021/nn900922z

Konečná, A., Venkatraman, K., March, K., Crozier, P. A., Hillenbrand, R., Rez, P., & Aizpurua, J. (2018). Vibrational electron energy loss spectroscopy in truncated dielectric slabs. *Physical Review B*, *98*(20), 205409. https://doi.org/10.1103/PhysRevB.98.205409

Kordahl, D., Alexander, D. T. L., & Dwyer, C. (2021). Waveguide modes spatially resolved by low-loss STEM-EELS. *Physical Review B*, *103*(13), 134109. https://doi.org/10.1103/PhysRevB.103.134109

Krivanek, O. L., Dellby, N., & Lupini, A. R. (1999). Towards sub-Å electron beams. *Ultramicroscopy*, *78*(1–4), 1–11. https://doi.org/10.1016/S0304-3991(99)00013-3

Krivanek, O. L., Lovejoy, T. C., Dellby, N., Aoki, T., Carpenter, R. W., Rez, P., Soignard, E., Zhu, J., Batson, P. E., Lagos, M. J., Egerton, R. F., & Crozier, P. A. (2014). Vibrational spectroscopy in the electron microscope. *Nature*, *514*(7521), 209–212. https://doi.org/10.1038/nature13870

Krivanek, O. L., Ursin, J. P., Bacon, N. J., Corbin, G. J., Dellby, N., Hrncirik, P., Murfitt, M. F., Own, C. S., & Szilagyi, Z. S. (2009). High-energy-resolution monochromator for aberration-corrected scanning transmission electron microscopy/electron energy-loss spectroscopy. *Philosophical Transactions of the Royal Society A: Mathematical, Physical and Engineering Sciences*, *367*(1903), 3683–3697. https://doi.org/10.1098/rsta.2009.0087

Lagos, M. J., Trügler, A., Hohenester, U., & Batson, P. E. (2017). Mapping vibrational surface and bulk modes in a single nanocube. *Nature*, *543*(7646), 529–532. https://doi.org/10.1038/nature21699

Liu, Q., March, K., & Crozier, P. A. (2017). Nanoscale probing of bandgap states on oxide particles using electron energy-loss spectroscopy. *Ultramicroscopy*, *178*, 2–11. https://doi.org/10.1016/j.ultramic.2016.06.010

Liu, Q., Quillin, S. C., Masiello, D. J., & Crozier, P. A. (2019). Nanoscale probing of resonant photonic modes in dielectric nanoparticles with focused electron beams. *Physical Review B*, *99*(16), 165102. https://doi.org/10.1103/PhysRevB.99.165102

Lucklum, R., Ke, M., & Zubtsov, M. (2012). Two-dimensional phononic crystal sensor based on a cavity mode. *Sensors and Actuators, B: Chemical*, *171–172*, 271–277. https://doi.org/10.1016/j.snb.2012.03.063

Luo, L., Pu, S., Tang, J., Zeng, X., & Lahoubi, M. (2015). Highly sensitive magnetic field sensor based on microfiber coupler with magnetic fluid. *Applied Physics Letters*, *106*(19), 193507. https://doi.org/10.1063/1.4921267

McCreery, R. L. (2001). Raman Spectroscopy for Chemical Analysis. In *Measurement Science and Technology* (Vol. 12, Issue 5). https://doi.org/10.1088/0957-0233/12/5/704

Morville, J., Kassi, S., Chenevier, M., & Romanini, D. (2005). Fast, low-noise, mode-by-mode, cavity-enhanced absorption spectroscopy by diode-laser self-locking. *Applied Physics B: Lasers and Optics*, *80*(8), 1027–1038. https://doi.org/10.1007/s00340-005-1828-z

Painter, O., Lee, R. K., Scherer, A., Yariv, A., O'Brien, J. D., Dapkus, P. D., & Kim, I. (1999). Two-Dimensional Photonic Band-Gap Defect Mode Laser. *Science*, *284*(5421), 1819–1821. https://doi.org/10.1126/science.284.5421.1819

Plotkin-Swing, B., Corbin, G. J., De Carlo, S., Dellby, N., Hoermann, C., Hoffman, M. V., Lovejoy, T. C., Meyer, C. E., Mittelberger, A., Pantelic, R., Piazza, L., & Krivanek, O. L. (2020). Hybrid pixel direct detector for electron energy loss spectroscopy. *Ultramicroscopy*, *217*(June), 113067. https://doi.org/10.1016/j.ultramic.2020.113067

Ramp, H., Clark, T. J., Hauer, B. D., Doolin, C., Balram, K. C., Srinivasan, K., & Davis, J. P. (2020). Wavelength transduction from a 3D microwave cavity to telecom using piezoelectric optomechanical crystals. *Applied Physics Letters*, *116*(17). https://doi.org/10.1063/5.0002160

Raza, S., Stenger, N., Pors, A., Holmgaard, T., Kadkhodazadeh, S., Wagner, J. B., Pedersen, K., Wubs, M., Bozhevolnyi, S. I., & Mortensen, N. A. (2014). Extremely confined gap surface-plasmon modes excited by electrons. *Nature Communications*, *5*(1), 4125. https://doi.org/10.1038/ncomms5125

Schaffer, B., Grogger, W., Kothleitner, G., & Hofer, F. (2010). Comparison of EFTEM and STEM EELS plasmon imaging of gold nanoparticles in a monochromated TEM. *Ultramicroscopy*, *110*(8), 1087–1093. https://doi.org/10.1016/j.ultramic.2009.12.012

Schatzl, M., Hackl, F., Glaser, M., Rauter, P., Brehm, M., Spindlberger, L., Simbula, A., Galli, M., Fromherz, T., & Schäffler, F. (2017). Enhanced Telecom Emission from Single Group-IV Quantum Dots by Precise CMOS-Compatible Positioning in Photonic Crystal Cavities. *ACS Photonics*, *4*(3), 665–673. https://doi.org/10.1021/acsphotonics.6b01045

Stuart, B. H. (2004). Infrared Spectroscopy: Fundamentals and Applications. In *Infrared Spectroscopy: Fundamentals and Applications*. John Wiley & Sons, Ltd. https://doi.org/10.1002/0470011149

Tiemeijer, P. C., van Lin, J. H. A., & de Jong, A. F. (2001). First Results of a Monochromized 200KV TEM. *Microscopy and Microanalysis*, *7*(S2), 1130–1131. https://doi.org/10.1017/S143192760003172X

Venkatraman, K., Levin, B. D. A., March, K., Rez, P., & Crozier, P. A. (2019). Vibrational spectroscopy at atomic resolution with electron impact scattering. *Nature Physics*, *15*(12), 1237–1241. https://doi.org/10.1038/s41567-019-0675-5

Wiener, A., Duan, H., Bosman, M., Horsfield, A. P., Pendry, J. B., Yang, J. K. W., Maier, S. A., & Fernández-Domínguez, A. I. (2013). Electron-energy loss study of nonlocal effects in connected plasmonic nanoprisms. *ACS Nano*, *7*(7), 6287–6296. https://doi.org/10.1021/nn402323t

Wu, Y., Li, G., & Camden, J. P. (2018). Probing Nanoparticle Plasmons with Electron Energy Loss Spectroscopy. *Chemical Reviews*, *118*(6), 2994–3031. https://doi.org/10.1021/acs.chemrev.7b00354

Yan, X., Liu, C., Gadre, C. A., Gu, L., Aoki, T., Lovejoy, T. C., Dellby, N., Krivanek, O. L., Schlom, D. G., Wu, R., & Pan, X. (2021). Single-defect phonons imaged by electron microscopy. *Nature*, *589*(7840), 65–69. https://doi.org/10.1038/s41586-020-03049-y

Yang, Z., Zhou, K., Liu, X., Tian, Q., Lu, D., & Yang, S. (2007). Single-crystalline ceria nanocubes: Size-controlled synthesis, characterization and redox property. *Nanotechnology*, *18*(18), 185606. https://doi.org/10.1088/0957-4484/18/18/185606

Yurtsever, A., Couillard, M., & Muller, D. A. (2008). Formation of Guided Cherenkov Radiation in Silicon-Based Nanocomposites. *Physical Review Letters*, *100*(21), 217402. https://doi.org/10.1103/PhysRevLett.100.217402

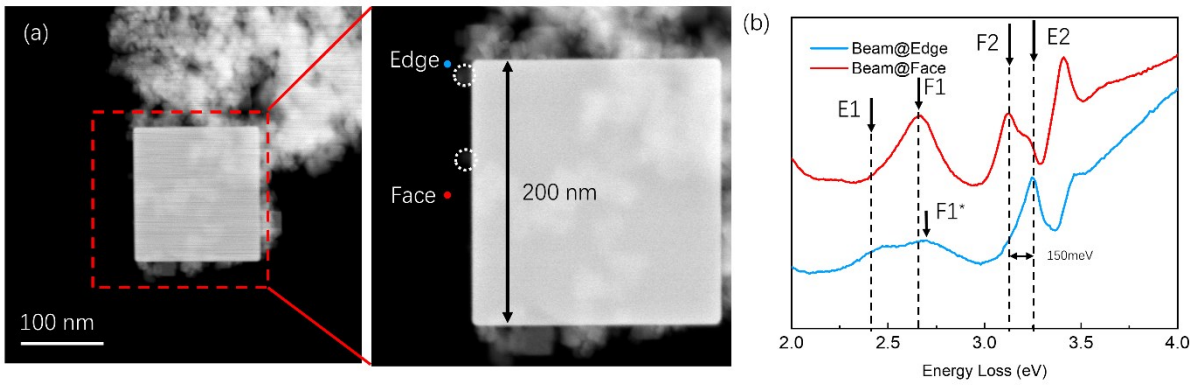

Figure 1 (a) STEM image of the cube and the position of the two points where the spectra were taken. The left face of the cube is nearly clean except for two tiny cubes, denoted by dotted circles. Both points are 10 nm away from the cube. (b) The background-subtracted energy-loss spectra at two points. The energy of the four peaks is indicated by arrows.

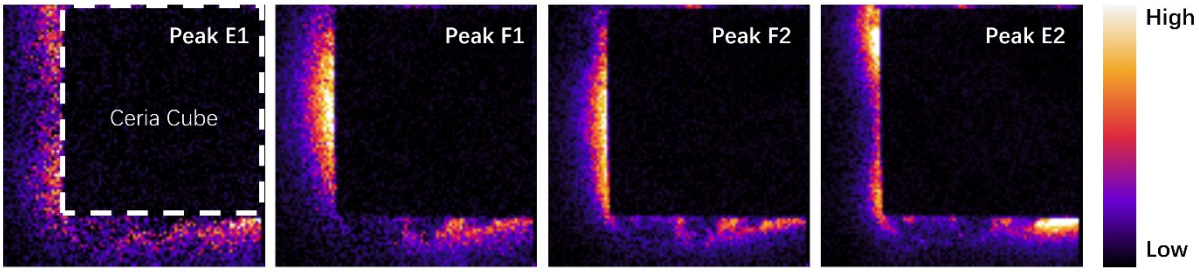

Figure 2 The EELS intensity maps associated with the bulk photonic modes of the cube. The white dotted box indicates the cube. The dark intensity in the cube is due to strong spectral attenuation by elastic scattering. The peak intensity is represented by the blackbody temperature of the color. Brightness and contrast of the four images are adjusted independently to highlight the spatial variation of each mode.

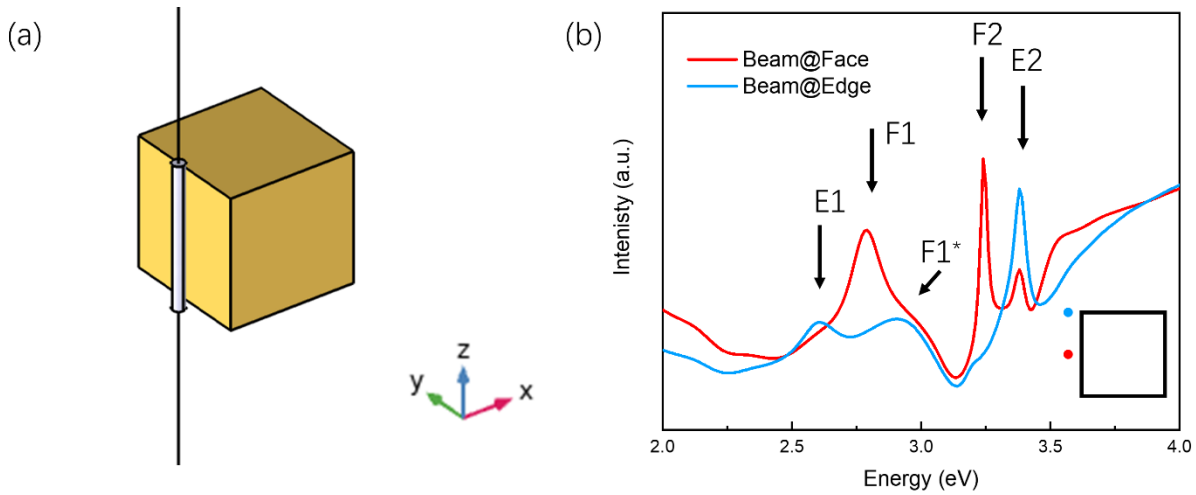

Figure 3 The simulation setup and the simulated energy-loss spectra. (a) The face setting scheme. The yellow ceria cube has the same size as the experimental cube (200nm). The vertical black line represents the electron beam. To increase the accuracy of calculation, the region near the cube and electron beam has a much finer mesh, which shows as a grey cylinder with a radius of 10nm close to the cube. (b) Simulated energy loss spectra. As the scheme at the right bottom shows, the blue curve stands for the calculated spectra when the beam is placed near the edge, and red curve is for the face setting.

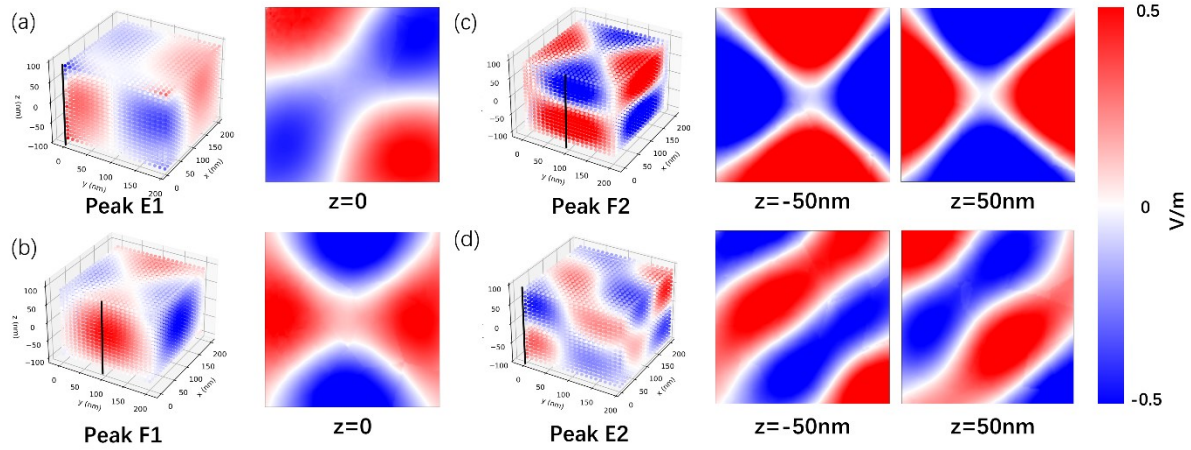

Figure 4 Z-component (parallel to the e-beam) of the electric field in the cube for each major peak. 3D plots demonstrate the electric field at the corresponding position as small circles with different colors. The position of the electron beam is represented by the black line. The cross-section of the cube at three different heights, i.e., z=-50nm, z=0, z=50nm, are also plotted here. On the left side (a-b) are the low energy peaks (E1, F1) and right side (c-d) are the high energy peaks (F2, E2).

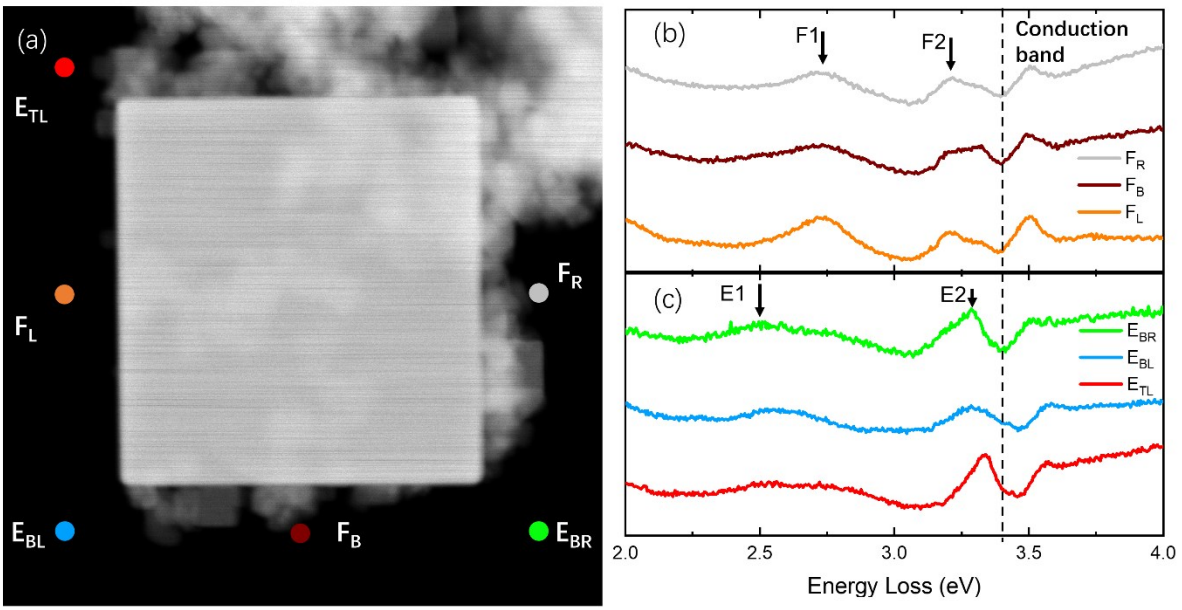

Figure 5 HAADF image and EELS point-scans extracted from EELS mapping at 2 set of geometrically equivalent points. (a) The 6 points are showed in the HAADF image. The three edge settings at **top-left**, **bottom-left**, and **bottom-right** of the cube are denoted by $\mathbf{E_{TL}}$, $\mathbf{E_{BL}}$, $\mathbf{E_{BR}}$, respectively. The three face settings at **left**, **bottom**, and **right** of the cube are denoted by $\mathbf{F_L}$, $\mathbf{F_B}$, $\mathbf{F_R}$, respectively. (b-c) Two set of spectra shows the energy loss spectra corresponding to each point. (b) presents the face settings and (c) presents the edge settings. All the spectra are normalized by zero-loss peak and plotted separately.

Supplementary material:

S1. EELS Background Subtraction and raw data

EELS background was subtracted using the power-law method in Digital Micrograph. We used two fitting windows to increase the accuracy. **Figure S1** demonstrates the raw data, fitting windows, and one of the subtracted data from **figure 1**. Notice that there are three gaps that have two-pixel width, pointed out by the arrow. These gaps are corresponding to the chip boundaries of the detectors.

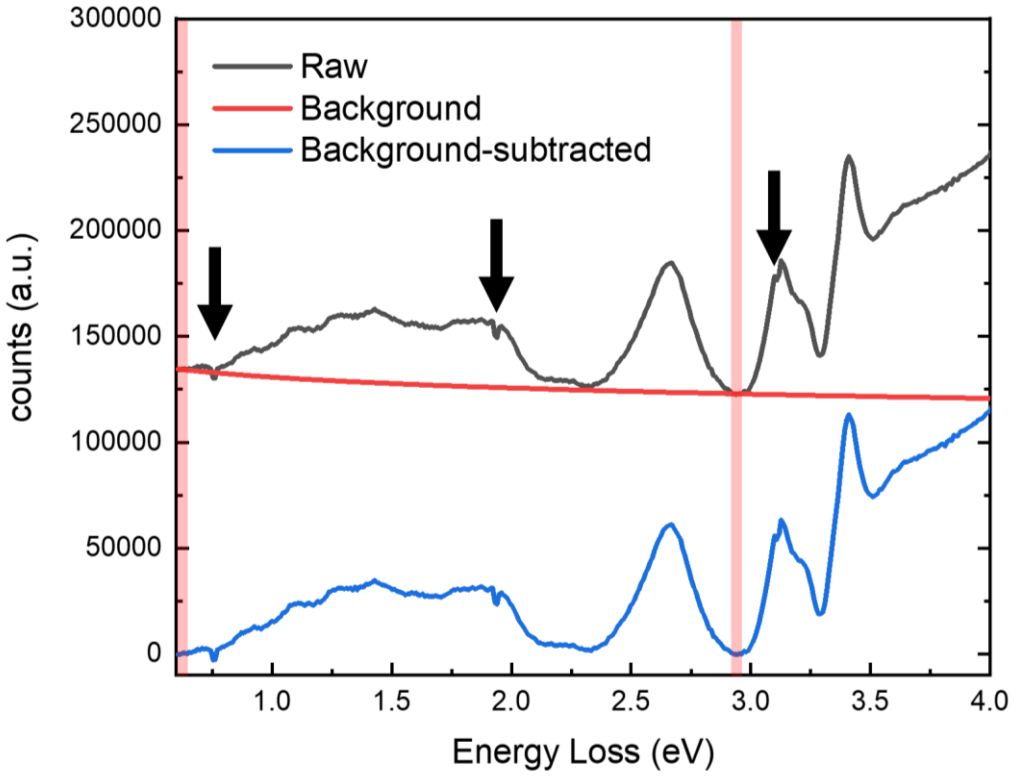

We used interpolation to correct these gaps for the data we presented in the paper.

Figure S1 Raw data and background subtraction. The blue area represents the raw data. The red boxes are the windows the program used to fit a power law background and red curve is the fitted background. The green area is the background-subtracted data that we present in the paper. Black arrows are pointing to the gap corresponding to chip boundaries of the detector.

S2. Spectra inside the cube

Although the elastic scattering largely suppressed the overall signal inside the cube, the photonic mode is still detectable. Here we sum the spectra inside the cube from the EELS map in **figure 2**. The area we select is ~5 nm away from the cube surface to avoid collecting signal from the surface. As shown in the **figure S2**, the peaks correspond to the modes, indicating by the arrow, are still visible.

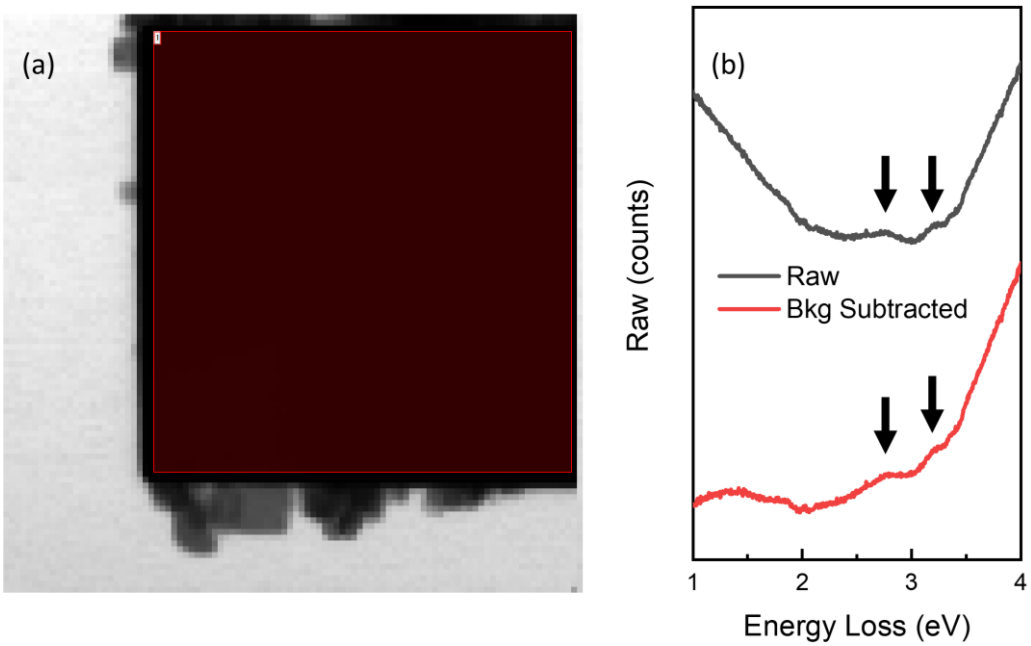

This further confirms that the effect is not a surface effect.

Figure S2 (a) Virtual BF image reconstructed from EELS mapping. The intensity of each pixel is corresponding to the ZLP intensity. The red box represents the area we used for summation. **(b)** Summation of the spectra. The black curve represents the raw spectra summation, and the red curve is the background subtraction result. Arrows are pointing to features corresponding to photonic modes.

S3. Solving the eigenmode equation

One way to find the numerical solution to the standing wave equation is by plot (**figure S3**). To find the x values that meet $f(x) = g(x)$, we can plot both function in the same coordinate, and the x coordinates of the intersection of will be the solution. Both x and y axis are in unit of energy. The straight line is the function at L.H.S., $f(E) = E$, where $E = \hbar\omega$. All the curves represent the R.H.S. of the standing wave equation with different k^2, $g(k^2, E)$. The intersect will be the solution to the equation.

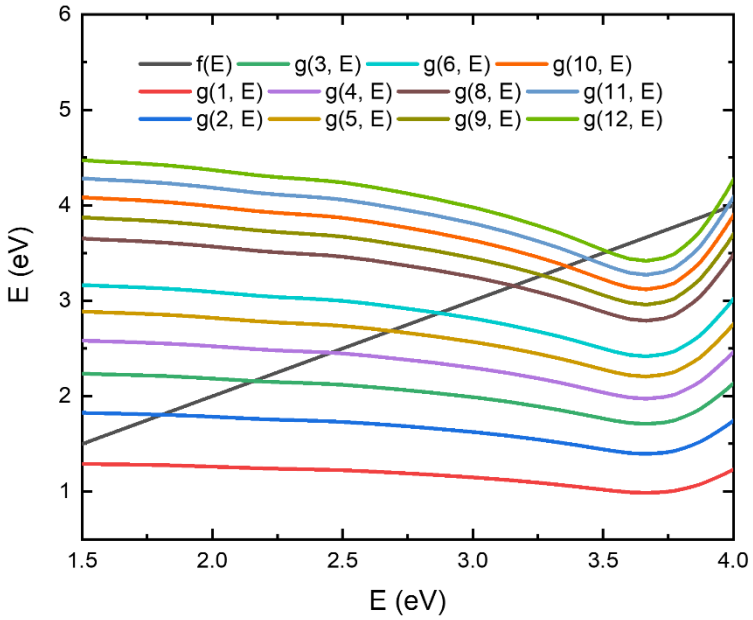

Figure S3 Solution to the eigen mode equation. The intersect between the black straight line and the curves represent the solution.

S4. Electric field subtraction generated from Cherenkov effect

Since the velocity of electron in TEM is very high (~0.55c) (**figure S4(a)**), we need to take relativistic effect into consideration, i.e., the Cherenkov radiation. By the criteria, when the velocity of moving charged particle $v_e > c_{CeO_2} = c/n_{CeO_2}$, where n_{CeO_2} is the refractive index of ceria, Cherenkov radiation emits and forms a cone shape, i.e., the Cherenkov cone. **Figure S4(c)** shows a V-shape electric field cone on the surface of the cube in simulation, which is corresponding to the Cherenkov. Although the field is coupled with photonic modes, we can still see a trend of Cherenkov cone.

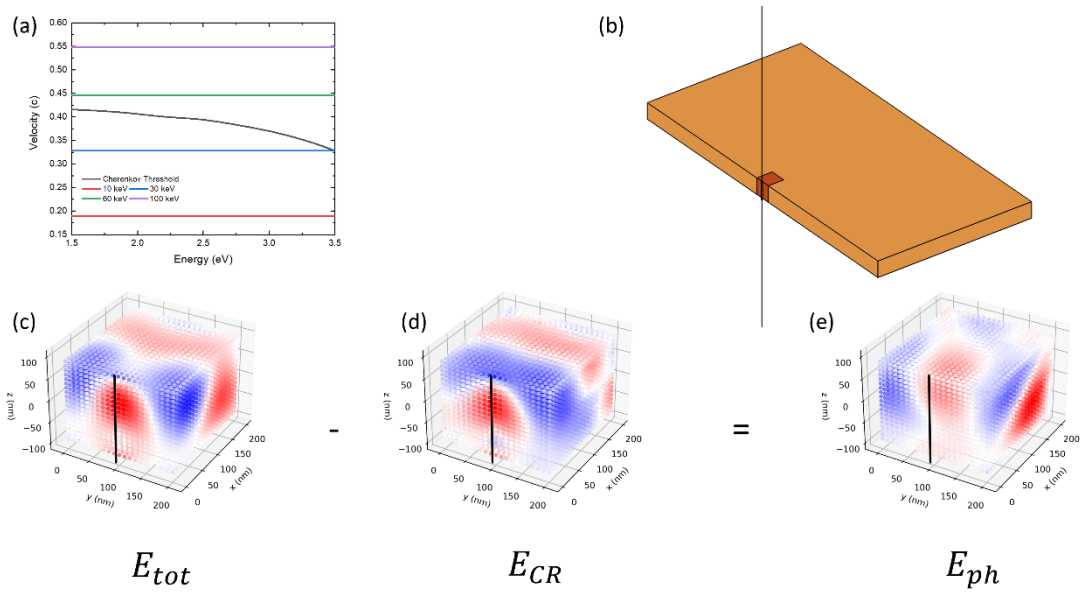

Figure S4 Demonstration of Cherenkov effect. (a) Cherenkov threshold for CeO_2. The horizontal lines are the calculated electron velocity (relativistic) of different acerating voltage. The black curve is the Cherenkov threshold corresponding to the dielectric function of CeO_2. (b) Demonstration and comparison of semi-infinite slab and the cube we used in our simulation. The large orange slab is the semi-infinite slab, and the red cube is the simulation cube in face excitation setting. (c-e) Electric field plot corresponding to total electric field, electric field caused by Cherenkov effect, and the electric field correspond to photonic modes. The black line represents the electron beam.

We assume that the electric field inside the cube only contains two parts: The part corresponding to photonic modes, E_{ph}, and the part corresponding to Cherenkov effect, E_{CR}. To minimize the contribution from Cherenkov radiation and let the field that represents the electric field stand out, a simple way is just subtract the field generated from Cherenkov effect. Therefore, we can calculate the electric field from Cherenkov effect from a model that has every setting the same as the cube model except the geometry (**figure S4(b)**). Here, we performed a simulation replacing the cube with a semi-infinite slab, with same thickness but much larger width and depth. By subtracting the electric field at the same point in two models (Shown as the red cube in **figure S4(b)**), we can get the electric field from the photonic mode approximately.

S5. Electric field in z-direction

Here we show the electric field of different peaks at different heights.

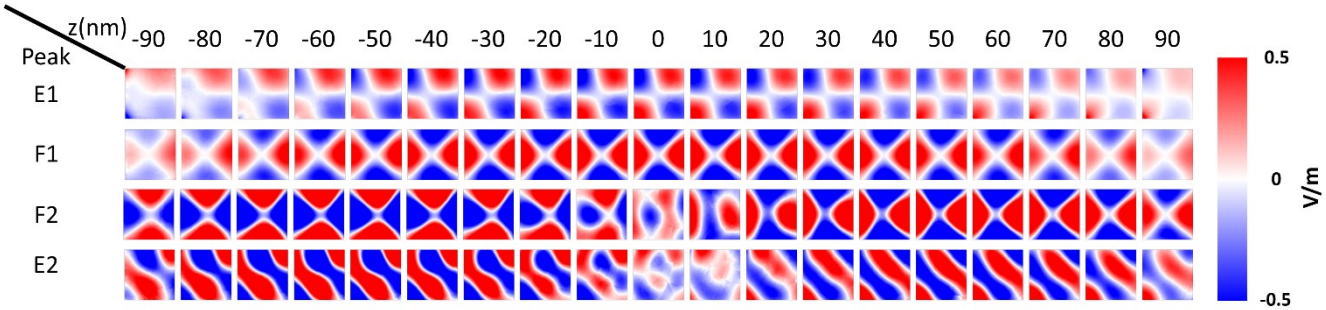

Figure S5 Electric field at different z-height for different peaks. Rows represent different peaks, and columns represent different height. All the graphs share the same color bar.